Nondimensional Parameter for Characterization of Wall Shear Stress From Underexpanded Axisymmetric Impinging Jets

Patrick Fillingham[1]
Department of Mechanical Engineering,
University of Washington,
Seattle, WA 98105

Harikrishnan Murali[1]
Department of Aeronautics and Astronautics,
University of Washington,
Seattle, WA 98105

Igor V. Novosselov[2]
Department of Mechanical Engineering,
University of Washington,
Seattle, WA 98105
e-mail: ivn@uw.edu

Wall shear stress is characterized for underexpanded axisymmetric impinging jets for the application of aerodynamic particle resuspension from a surface. Analysis of the flow field resulting from normally impinging axisymmetric jets is conducted using computational fluid dynamics (CFD). A normally impinging jet is modeled with a constant area nozzle while varying the height to diameter ratio (H/D) and the inlet pressures. Schlieren photography is used to visualize the density gradient of the flow field for validation of the CFD. A dimensionless jet parameter (DJP) is developed to describe flow regimes and characterize shear stress. The DJP is defined as being proportional to the jet pressure ratio divided by the H/D ratio squared. Maximum wall shear stress is examined as a function of DJP with three distinct regimes: (i) subsonic impingement (DJP < 1), (ii) transitional (1 < DJP < 2), and (iii) supersonic impingement (DJP > 2). It is observed that wall shear stress is limited to a finite value due to jet energy dissipation in shock structures, which become a dominant dissipation mechanism in the supersonic impingement regime. Additionally, the formation of shock structures in the wall flow was observed for DJP > 2, resulting in difficulties with dimensionless analysis. In subsonic impingement and transitional regimes, equations as a function of the DJP are obtained for the maximum wall shear stress magnitude, maximum shear stress location, and shear stress decay. Using these relationships, wall shear stress can be predicted at all locations along the impingement surface. [DOI: 10.1115/1.4037035]

1 Introduction

Impinging jets are used for a wide range of engineering applications which include the cooling of electronic components, surface cleaning in the microelectronic industry, and annealing processes. Particularly, noncontact particle removal is of great interest in the field of trace material detection as it allows for the rapid collection of the sample superior to traditional swabbing methods. Aerodynamic noncontact sampling provides an interesting, yet challenging, solution to this problem. Although not related to particle sampling, the behavior of impinging jets has been studied extensively for the application of vertical aircraft takeoff. These studies are associated with the underexpanded jets with exit pressure of at least 1.87 times the ambient pressure. These jets are accompanied with high pressures as they impinge on the surface and can produce high wall shear stress in the wall jet region. This shear stress is critical in dislodging particles from the surface.

The basic structure of the impinging jet is shown in Fig. 1. It is comprised of three characteristic regions that include the free jet region (under the nozzle), the stagnation zone (the point of contact with the plate), and the wall jet region along the plate. As the jet is underexpanded, it expands further outside the nozzle through a number of expansion and compression waves. This region of the flow is contained within the potential core in its free jet region and along with it, is a set of acoustic feedback loops formed on impingement against the plate. Henderson and Powell [1], Krothapalli et al. [2], and Tam and Ahuja [3] are among the researchers who have examined the acoustics of impinging jets.

The experimental studies by Donaldson and Snedeker [4] using Schlieren give a clear insight into the complex shock structure of the supersonic jet. They examined the shock structure development and concluded that it primarily depended on the nozzle pressure ratio and the standoff distance of the jet. For a free jet without an impingement plate, the oblique shocks alone expand the flow and render the flow subsonic. This is seen in impinging jet configurations with high standoff distances. However, in some jet configurations, the airflow onto the plate may still be supersonic, and this leads to the formation of a normal shock ahead of the plate. Across this shock, the flow transitions to subsonic and is
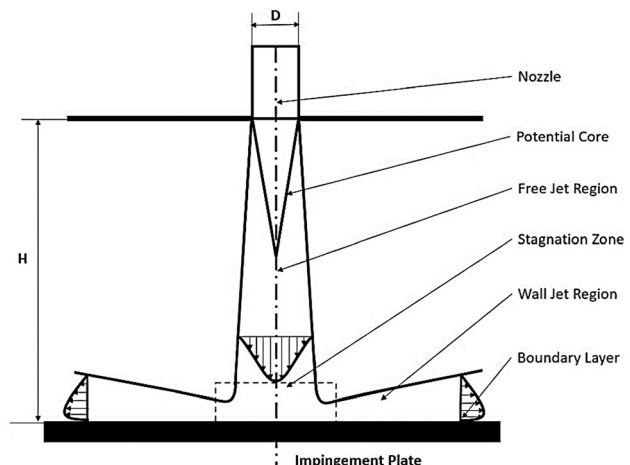

Fig. 1 Schematic diagram of a normal impinging jet. The flow consists of the free jet region, stagnation zone, and wall jet region. The boundary layer develops as jet impinges on the surface and creates the flow parallel to the surface.

deflected to the wall jet region along the plate. For higher standoff distances, maximum pressure occurs at the centerline of the jet on the impingement plate. For very small standoff distances, researchers have observed the formation of a stagnation bubble at the impingement region [5]. For these cases, the maximum pressure was observed to occur off the center.

A great deal of computational research has been done in regard to the supersonic impinging jet. Most of the computational fluid dynamics (CFD) studies in this field [6–8] have employed the Reynolds-averaged Navier–Stokes models, which used lesser computational memory and time to yield good predictions with respect to the experimental data. Alvi et al. [6], looked at solving for the flow field using different turbulence models and compared them to experimental velocity measurements. They used $k - \omega$ shear stress transport (SST) and Spalart Allmaras with curvature correction and observed that they produced nearly identical results. While these studies are comprehensive and important to the understanding of underexpanded impinging jets, there is a lack of investigation into the wall jet region and, specifically, the wall shear stress developed along the plate.

The problem has been investigated for subsonic and mildly sonic jets experimentally in the past. Young et al. [9] used oil-film interferometry to measure the shear stress from a supersonic impinging jet. The experiment was limited to a single jet pressure ratio and can, therefore, draw no conclusions on the effect of pressure on the flow characteristics of the impinging jet and on the wall shear stress, as well as the limits of the scope of the results to mildly sonic jets. Tu and Wood [10] conducted a comprehensive study of wall shear stress developed from a subsonic impinging jet, but their conclusions cannot be extrapolated to account for supersonic and compressible effects.

Smedley et al. [11] and Phares et al. [12] investigated a normally impinging jet on a glass plate containing microspheres and used the previous results of theoretical shear stress profiles, adhesion forces, and particle removal rates to infer shear stress along the plate. They determined that the maximum shear stress was directly related to the Reynolds Number of the jet and was directly proportional to the height to diameter ratio (H/D) ratio. They also concluded that the axial location of the maximum shear will be located at $r/H = 0.09$ for all cases of the jet with $H/D > 8$. Their results find shear stress to be directly related to particle forces, but do not account for compressibility and turbulent effects. These conclusions were produced for subsonic and nearly sonic jets and its applicability for highly underexpanded jets, where the flow is compressible in the wall jet region, is uncertain. Shear stress is the correct parameter to analyze, but it must be used along with the entire boundary layer profile to comprehensibly understand the forces acting on the particle.

Even with full confidence in the results discussed above, it still has been shown that the shear stresses obtained for the jets examined in these experiments and models do not reach the critical shear stress needed for the successful removal of typical explosive particles. Keedy et al. [13], using the model of Birch et al. [14] for the virtual origin of underexpanded jets as their jet parameter (i.e., the origin of hyperbolic velocity decay, coinciding with incompressible flow), demonstrated that explosive particles will only be removed if the impingement plate is within the distance of the virtual origin. The scenarios of interest have been extrapolated using a Mach number correction by Smedley et al. [11], but have not been investigated directly. Further investigation into underexpanded jets is necessary to determine the parameters of the impinging jet required to obtain the levels of shear stress needed for particle removal.

For subsonic jets, the shear stress profile will collapse on a single normalized location line, and the maximum shear stress will be directly related to the Reynolds number of the jet; however, this has not been demonstrated for a wide variety of supersonic impinging jets. It is thus desirable for design and further experimentation to determine a single jet parameter for maximum shear stress, and the decay of shear stress along the wall. Using a simple

fully developed nozzle, the problem has been simplified to be applied for design applications. Past equations from Phares et al. [12], Smedley et al. [11], Tu and Wood [10], as well as the model developed by Birch et al. [14] (used by Keedy et al. [13]) have been based on the Reynolds number and average exit velocity of the jet, which are much more difficult to control for than just the pressure ratio and H/D.

Previously developed models do not address the relationship between the impinging jet parameters and the shear stress on the impingement surface required to gain insight into the forces acting on the particles in the flow boundary layer. Ideally, such a model would include a nozzle gauge pressure, a nozzle geometry (size and shape), the stand-off distance, and the jet impingement angle and jet duration. In this paper, we will address the development and validation of the model for impingent of the normal underexpanded jet with a fixed nozzle geometry, specifically, the effect the nozzle gauge pressure, nozzle diameter, and its standoff distance on the wall shear stress.

2 Methodology

The presented work is aimed at the characterization of wall shear stress resulting from the impingement of the normal axisymmetric jet and includes both numerical and experimental studies. Our research methodology consists of: (i) the development of the CFD model for an underexpanded air jet, (ii) the validation of the numerical results by comparison with Schlieren images, and (iii) the analysis of the CFD results to determine wall shear stresses over operational parameters of interest. Our numerical and the experimental matrix contain two jet parameters: nozzle pressure and the H/D. Only normal jets were considered in this study; a straight pipe with fully developed flow is used as a nozzle. We thus developed a dimensionless jet parameter that quantifies the wall shear stress for any location on an impingement surface for a wide range of pressure ratios and H/D combinations.

2.1 Computational Fluid Dynamic Study. A computational study provides an insight into the flow field with all its necessary characteristics: shock structures and the velocity field near the wall; this is a simple, yet effective, way to calculate wall shear stresses for a range of operational parameters. The computational analysis is performed using the commercial software code ANSYS FLUENT 16.2 and a cell centered finite volume approach. The steady-state Reynolds- and Favre-averaged Navier–Stokes equations are solved to obtain the flow field.

Computational fluid dynamic solvers can be classified as two distinct families of schemes: pressure-based and density-based methods. Previously, pressure-based methods were created for incompressible flows and flows with low Mach number flows, while the density-based methods have typically dominated transonic and supersonic simulations encountered in traditional aerodynamics applications. In the pressure-based method, a pressure equation is derived from the continuity and the momentum equations in such a way that the velocity field, corrected by the pressure, satisfies the continuity. Whereas for the density-based solver, the solver solves the governing equations of continuity, momentum, and (where appropriate) energy and species transport simultaneously. Typically, the pressure-based solver was created for incompressible flows. But it has been modified through the introduction of pressure–velocity coupling, which solves for pressure from the continuity and momentum equations, taking into consideration the effect pressure has on both the velocity and density [15]. This coupling uses either a pressure-based segregated algorithm or a coupled algorithm. The pressure-based coupled algorithm offers superior performance to the segregated algorithm and also aids with better numerical convergence. This forms an alternative to the density-based solver. Although nearly all numerical simulation cases in this work include the supersonic region $Ma > 1$, where density solver may be beneficial, the majority of the flow in the wall jet region is subsonic. Thus, the use of the coupled pressure-based solver is more appropriate for
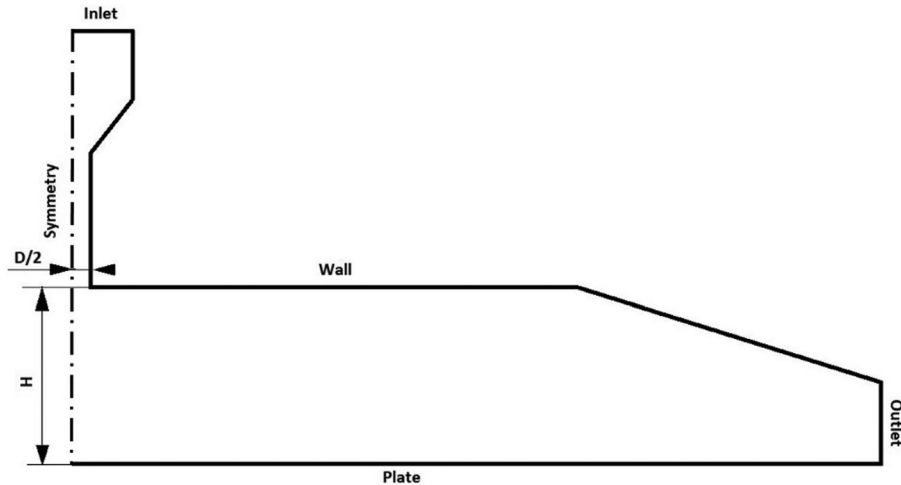
Fig. 2 Computational domain (not to scale). Note that only half the domain is modeled due to the presence of symmetry. The inlet is supplied with gauge pressure, plate follows the model of a no slip wall, and outlet represents the open atmosphere (0 psig).

this study [16]. A second-order scheme was used for the pressure, whereas a third-order monotonic upstream-centered scheme for conservation laws scheme was used for density, momentum, and turbulence, which was necessary to avoid the effects of numerical viscosity (associated with the first-order schemes) on the jet dissipation, as well as pressure–strain relationship. Since the flow is also associated with changes in temperature, the Sutherland model, which is based on the on kinetic theory of ideal gases and an idealized intermolecular-force potential, is used for viscosity.

The choice of the turbulence model takes into account the need to accurately capture the wall shear stress. Since the main focus of this analysis was on the wall jet region, we needed a model that resolves the viscous boundary layer well. The standard $k - \omega$ model suffered from errors around the near wall region, which was resolved using the modified $k - \omega$ SST model [17]. According to Catalano and Marcello [18], as $k - \omega$ SST is less stiff, it requires less computational effort. Based on the study by Alvi et al. [6], the $k - \omega$ SST model showed results quite similar to the actual data obtained. Hence, the most suited option based on an accurately resolved flow field was the $k - \omega$ SST model.

A schematic diagram of the computational domain is shown in Fig. 2 which is used for simulations taking advantage of the jet's axial symmetry. The nozzle radius ($D/2$) and the standoff distance to the impingement surface (H) were varied depending on the case. The converging section of the top wall does not represent the exact experimental setup, but was introduced into the CFD to aid with the solution convergence by minimizing the exit plane flow recirculation. This converging section has very low velocities, and, as a result, does not change the boundary layer properties in the vicinity of the area of study.

The mesh primarily comprises of quadrilateral elements, and for the majority of simulations, after conducting mesh independence studies, the size of the mesh is around 250,000 elements. To obtain the wall shear stress, the near wall properties have to be captured, and this is done by resolving the wall viscous sublayer. The viscous sublayer is of a thickness of $y^+ = 5$. To resolve this, at least three cells have to be placed within this region, so that the mesh at the impingement surface is created such that its first grid point is located at a distance of $y^+ \approx 1$. The typical size of an element within the impinging surface is of the order of 1 μm. For the boundary conditions, the inlet of the domain is supplied with air at a specific gauge pressure measured experimentally by a pressure transducer. The impinging jet is kept open to the air, and to model this, the outlet is kept far away from the inlet and is forced to be at atmospheric pressure (zero-gauge pressure). The axis of symmetry is conditioned to have no crossflow across it, and the walls are modeled as nonslip boundary.

2.2 Experimental Setup. The greatest uncertainties in the CFD simulations are the length and the structure of the supersonic jet region and the interaction of the supersonic jet with the impingement plate. While there are several publications describing the interaction between the supersonic jet and the surface, these are limited to a few H/D ratios and the jet pressures [7]. To perform any meaningful comparisons between the CFD and the experimental fluid dynamics, we have designed and performed a series of flow visualization experiments (Fig. 3).

A normal impinging jet system was built on the optical table. Two long constant diameter nozzles are used to allow for the flow to fully develop, while the standoff distance and pressure are adjusted to match the designed parameters. The pressure is then controlled by a regulator connected to conditioned shop air (RH ∼ 0%). The timing is controlled by a solenoid valve operated by an arbitrary function generator. The 1-s pulse width was used in this study. The pressure transducer downstream of the solenoid valve is used to measure the pressure in the nozzle. This nozzle pressure was then matched to the CFD boundary conditions as the inlet nozzle pressure. In the experiments, the nozzle was at a fixed location, and the location of the impingement plate was adjusted to the desired H/D for the impinging jet.

Schlieren imaging was used to visualize the flow patterns of the impinging jet. Schlieren imaging uses the refraction of light through media of variant density to visualize the density gradient of compressible flow. For our visualization, a z-type Schlieren setup was implemented. A halogen light bulb with a focusing lens and an optical slit were used as a point light source with spherical mirrors to collimate the light rays through the test section and to refocus the light onto a razor's edge, which blocks the refracted rays, allowing the camera to capture an image of the density gradient [19].

3 Results

3.1 Computational Model Validation. The supersonic underexpanded jet is associated with a series of expansion waves at the exit of the nozzle, and may also be accompanied by a plate shock based on the ratio of the standoff distance of the jet to its diameter (H/D ratio). These formations are characteristics of the underexpanded jet and hence validation of the CFD model would be obtained through an accurate prediction of the behavior in the under-expanded (supersonic) region of the jet—specifically, within the interaction between the shock wave pattern in the presence of the wall (Figs. 4 and 5).

To examine the capabilities of the numerical simulation to reproduce the features of the flow, the CFD results are compared
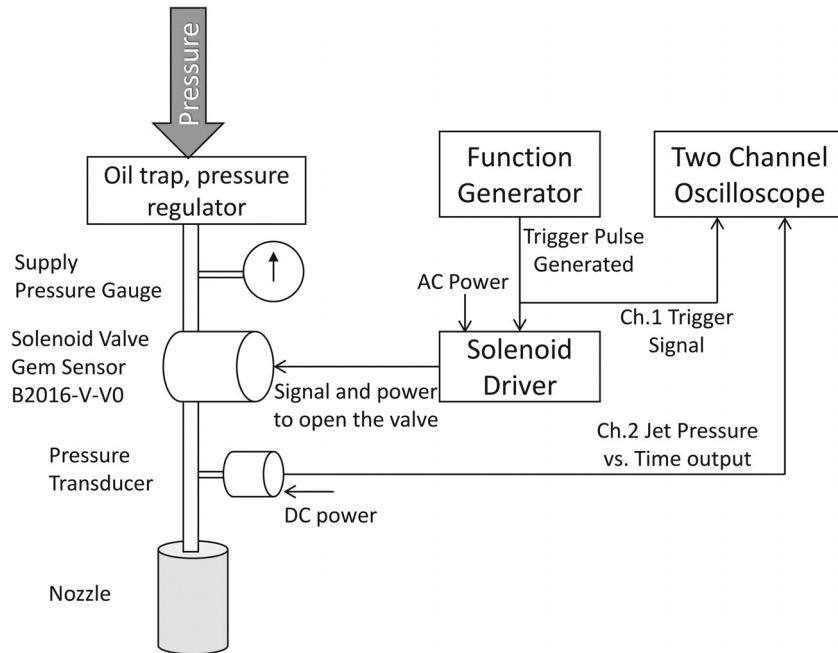
Fig. 3 Schematic of experimental impinging jet setup. Supply pressure was regulated through the supply pressure gauge and measured precisely using an electronic pressure transducer. The flow was regulated using an alternating current solenoid. The flow field was then captured using Schlieren imaging.
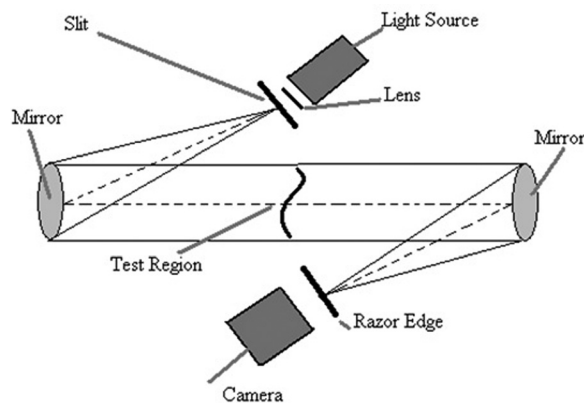

Fig. 4 Schematic of the z-type Schlieren setup used to visualize the flow field of the underexpanded impinging jet

with the experimental data (in this case, Schlieren images). Thus, for the purpose of validation, the numerical simulation was run for the case of the H/D ratio of 5, with three different inlet pressures and their density contours compared against their Schlieren counterparts as shown in Fig. 6.

The Schlieren images align quite well with the CFD contours. Similar results were obtained for an H/D of 10, but are omitted in the interest of brevity. The shock cells seem to decrease in number, but increase in strength as the inlet pressure is increased. As the H/D ratio is increased, more shocks cells formed in the free jet region. This comparison confirms that the chosen simulation approach is the appropriate tool for evaluating flow field for an underexpanded impinging jet.

3.2 H/D Parameter Verification. The z-type Schlieren setup was used to examine the flow field of impinging jets of two different diameters and across a variety of pressure ratios to affirm the previously determined self-similarity parameter of impingement height divided by jet diameter (H/D).
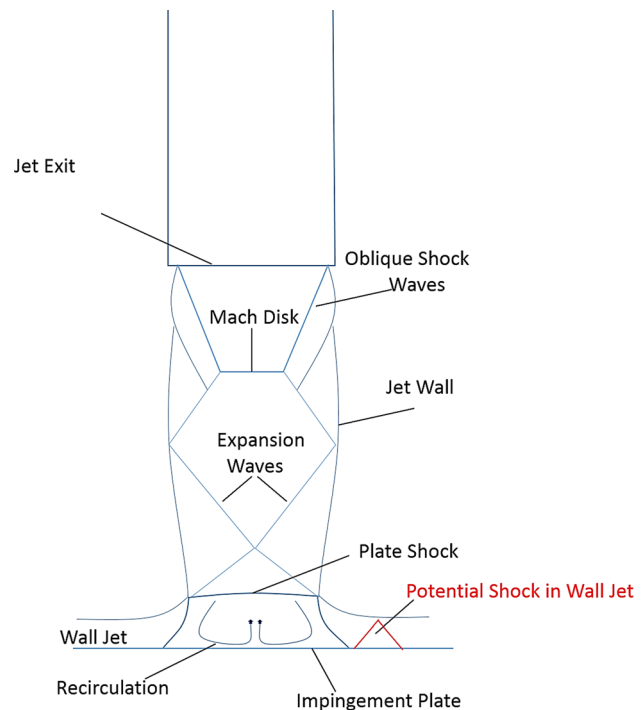

Fig. 5 Schematic of underexpanded impinging jet. Key characteristics are outlined. The presence of supersonic flow extending to the impingement point results in a normal plate shock, which dissipates energy resulting in less efficient removal. If the pressure in the recirculation zone is high enough a shockwave in the wall jet region may form.

The images from Fig. 7 confirm the self-similarity of impinging jets using the height to diameter ratio. For each case of different pressure ratios, the relative size, location, and number of shocks are identical.
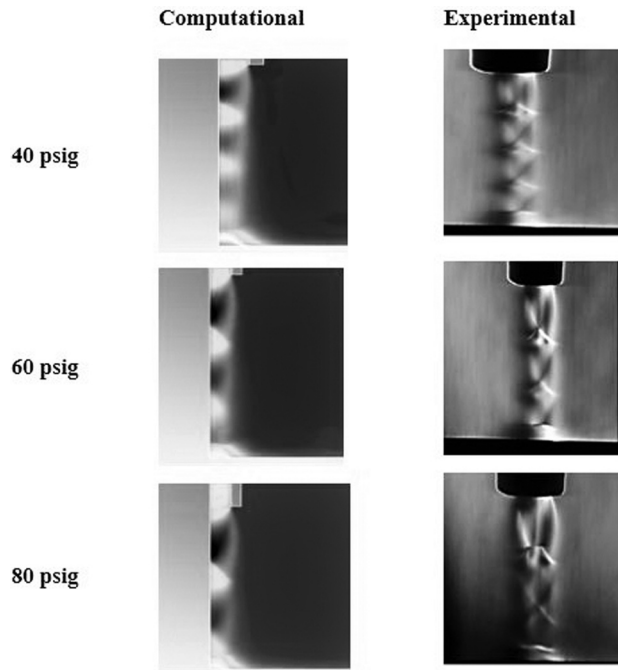
Fig. 6 Density contours of CFD model and Schlieren images at a height to diameter ratio of 5. The number of shock cells decreases with increasing pressure, but they get stronger. The oblique shock cells and the plate shocks produced by CFD are in agreement with the Schlieren images.
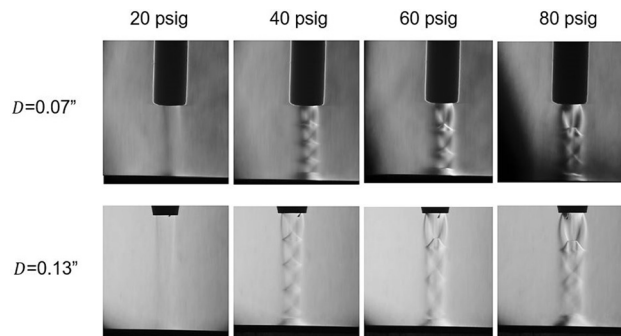
Fig. 7 Experimental verification of *H/D* as a similarity parameter. Normally impinging jets of similar *H/D*, supplied with the same inlet pressure, produce the same flow pattern.

Previous researchers and the Schlieren images in Fig. 7 have helped identify *H/D* as a similarity parameter. To be confident moving forward, the CFD model is used to verify *H/D* similarity by looking at the wall shear profiles for different jets with the same *H/D* ratio. Figure 8 plots the profile of shear stress along the impingement plate for several different diameters with the height adjusted to maintain the same *H/D*.

Figure 8 shows that the shear stress profiles are not identical across the three different jet diameters (changing the impingement height to keep the *H/D* constant), as was expected. After further investigation, changing the diameter while fixing *H/D* does not affect the location of the maximum sheer stress or how the sheer stress decays along the impingement surface. This means that when adjusting for diameter only the magnitude of the shear stress must be accounted for. It was found that the maximum wall shear value for constant pressure and *H/D* scales with the inverse of the fourth root of the diameter such that:

$$\frac{\tau_a}{\tau_b} = \left(\frac{D_b}{D_a}\right)^{\frac{1}{4}} \qquad (1)$$

The dependency of wall shear stress on jet diameter and height independently of the *H/D* ratio is likely due to subtle differences in turbulent dissipation as well as differences in the inherent change in viscosity from the jet exit to the surface due to the temperature drop occurring from the jet exit to the impingement surface. Determining the physical mechanisms responsible for the effect of diameter on wall shear stress is beyond the scope of this paper and thus for this work will be dealt with by the adjustment in Eq. (1). Moving forward all simulations were conducted for a diameter of 2.12 mm, and all equations may be adjusted appropriately to specific applications.

3.3 Wall Shear Stress Analysis. On establishing confidence in the CFD model, 40 separate cases are run, which span eight different *H/D* ratios (5, 10, 15, 20, 25, 30, 40, and 60) and five separate jet pressures (20:20:100 psig). Initially, the wall shear stress profiles were examined for all cases to understand the overall trends. Figure 9 shows these profiles for three *H/D* ratios across all pressures, by plotting τ against a normalized distance along the plate of the radial distances divided by the impingement height (*r/H*).

The effect of the increasing pressure ratios and increasing *H/D* on the wall shear is visible through Fig. 9. As the inlet pressure is increased, the wall shear stress along the plate increases. And, similarly, wall shear stress is seen to increase as the standoff distance to the plate is decreased. Among the two parameters, the effect produced by changing *H/D* on the wall shear stress is greater than that caused by the inlet pressure, i.e., the decrease in *H/D* produces a larger increase in the wall shear than that produced by increasing the inlet pressure. This pattern is noted for all cases until supersonic flow begins to appear at the wall jet region, which is seen in Fig. 9 for *H/D* = 10 and pressures of 80 psi and 100 psi.

It is immediately noticeable for supersonic impingement that the location of the max shear is not consistent with regards to *r/H* as was found for subsonic jets [9,11,12]. There is a clear effect of pressure, as well as *H/D*, on the location of the maximum shear stress. This is especially true for the *H/D* = 10 case. For this case, supersonic flow is present in the wall jet region of the flow. The effect of the supersonic flow along the wall jet region is difficult to characterize and is thus beyond the scope of this paper.

The goal of this research is to easily characterize the wall shear stress based upon the impinging jet parameters. When analyzing the trends, it was found that the peak wall shear can be directly related to a single dimensionless jet parameter. We found that the maximum wall shear stress value tended to go as the inverse of $(H/D)^2$ and is directly proportional to the ratio of the jet gauge pressure over the atmospheric pressure. We then investigated how to appropriately adjust the *H/D* ratio to obtain a certain shear stress at a variety of pressure ratios. Consistent with our expectations, if the pressure is decreased by a factor of *X*, then in order to achieve the same wall shear stress, the *H/D* must be decreased by a factor of $\sqrt{X}$.

This led us to develop the dimensionless jet parameter

$$\text{DJP} = \frac{\alpha * \left(\frac{P_{\text{gauge}}}{P_{\text{atm}}}\right)}{\left(\frac{H}{D}\right)^2} \qquad (2)$$

where $\alpha = 46.3$ normalizes, from zero to one, the range where the DJP can be accurately used to characterize the impinging jet. The physical representation of DJP = 1 is that the length of the supersonic region of a free (nonimpinging) jet at the given pressure ratio would be at the standoff distance of the jet.

Figure 10 displays all scenarios of the underexpanded impinging jet examined for this work. The three distinct regimes can be seen clearly in Fig. 10. An exponential trend line is developed in
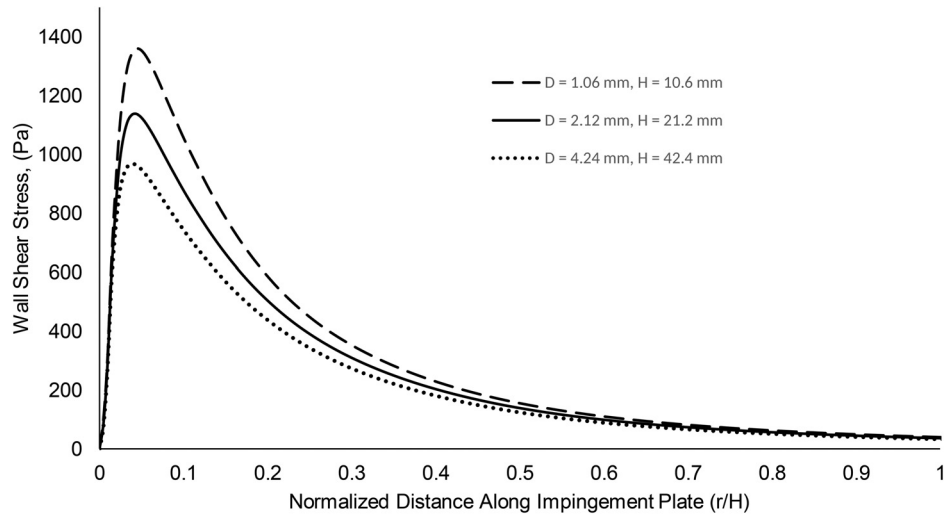
Fig. 8 Experimental verification of *H*/*D* as a similarity parameter. Normally impinging jets of similar *H*/*D*, supplied with the same inlet pressure of 40 psi, produce the same shear stress profiles but different maximum values.
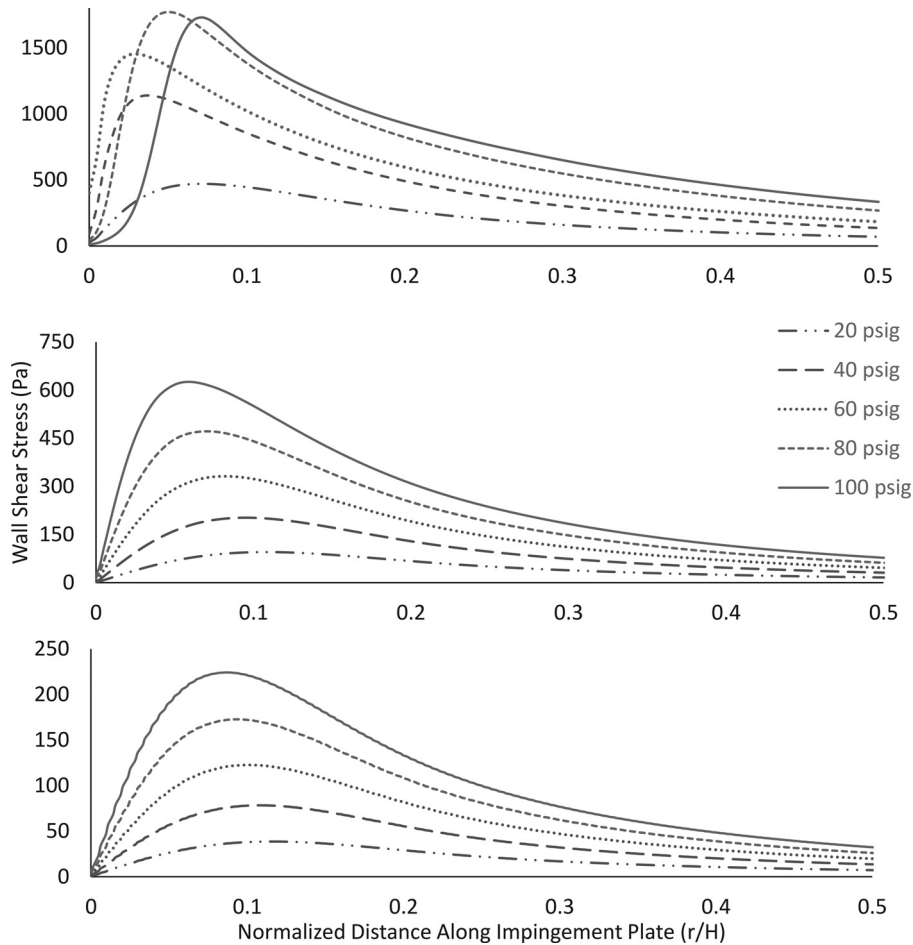

Fig. 9 Wall shear stress distribution for *H*/*D* of 10, 20, and 30 at gauge pressures of 20, 40, 60, 80, and 100 psig. The plots show the change in maximum wall shear stress magnitude and location.

Eq. (3) to capture the entire range of DJP's. This trend is not accurate enough to be used for small values of DJP, but works in the transitional regime, capturing the maximum value in the supersonic impingement regime

$$\tau_{\max} = 1780\left(1 - e^{-(0.775*\text{DJP})^{1.57}}\right) \tag{3}$$

When removing the data points with DJP greater than unity, a more accurate trend can be defined with a second-order
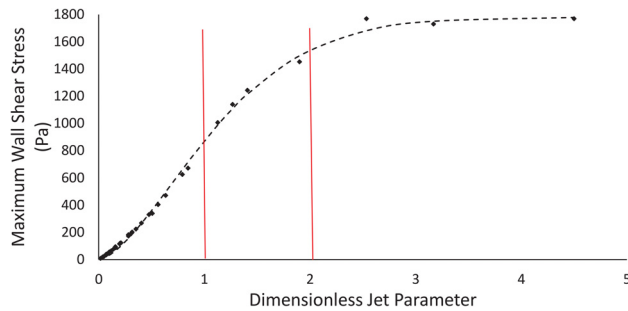
Fig. 10 Maximum wall shear stress versus DJP with lines separating the subsonic, transitional, and supersonic wall regions. For DJP greater than 1, the maximum shear stress asymptotically approached the maximum value limit.

Fig. 12 Plot showing the effect of the dimensionless jet parameter on the peak wall shear location

polynomial fit. For comparison, we plotted our models with the equation for maximum shear stress using the Mach number correction developed by Phares et al. [12].

It is clear that the results from Phares et al. [12] cannot be consistently extended to underexpanded impinging jets. Using the dimensionless jet parameter, we can accurately determine the maximum shear stress from underexpanded impinging jets using a single quadratic trend line equation as shown in Fig. 11 with Eq. (4). The trend was expected to be linear, but at the higher pressures and smaller H/D, the flow is compressible along the impingement plate, and these effects are most likely responsible for the second-order relationship. The trend represents all of the data for DJP < 1 within 5% of the computed value

$$\tau_{max} = 327.01 * DJP^2 + 526.98 * DJP \qquad (4)$$

For the application of particle removal, it is important not only to know what the maximum shear will be, but also the location of the maximum and the rate of decay of the shear stress along the impingement plate. In the subsonic impingement regime, the square root of the DJP was shown to be linearly related to the location of the maximum shear normalized by the impingement height of the jet. In the transitional and supersonic impingement regimes, the max shear location was shown to move inside the radius of the jet and becomes unpredictable using the DJP (Fig. 12).

To better represent the physics of the impinging jet, the radius of the jet is subtracted from the radial location of the max shear. The trend line for the max shear location is given by Eq. (5). As the DJP goes to zero, the peak location approaches the tangent of 7.5 deg, which is the spreading angle for subsonic jets, thus being the limit for the location of the maximum shear. It should also be noted that as the length of the supersonic region approaches the
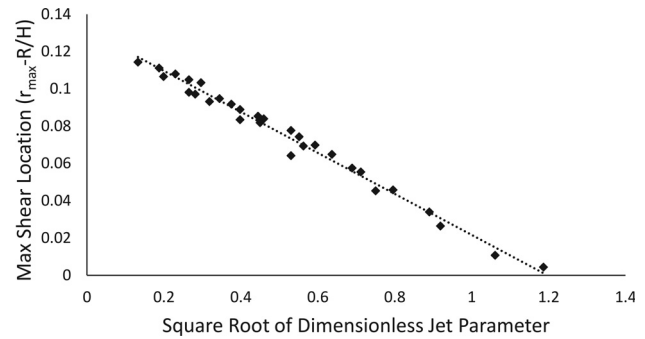
impingement height, the location of the max shear approaches the radius of the jet. This is due to the fact that the supersonic region of the jet does not expand as the subsonic region does. The compressibility of the air at high velocity is responsible for the shifting of the maximum shear location toward the impingement point as DJP increases

$$\frac{(r_{max} - R)}{H} = \tan(7.5 \text{ deg}) - 0.11 * \sqrt{DJP} \qquad (5)$$

Now, that we can locate the maximum wall shear, we can determine how the shear decays along the plate. We define a new variable r^*, where $r^* = 1$ at the location of the maximum shear for each case, and zero at the center of the impingement point of the jet

$$r^* = \frac{r}{r_{max}} \qquad (6)$$

Using the r^* variable, we can then characterize the decay of the shear stress along the plate. A $(1/r^{*2})$ relationship was initially assumed for the decay, but it was found that an exponential decay more accurately depicts the decay of the shear stress. We then use an equation to characterize the shear stress away from the peak location

$$\tau = \tau_{max} * e^{\beta(1-r^*)} \qquad (7)$$

Using Eq. (7), β was optimized for minimum error in the shear stress profile for each case run on our model. It was found that β is also directly related to the DJP. We could then come up with a trend for β and thus have the ability to determine shear stress along all of the locations of the plate based solely on the dimensionless jet parameter.
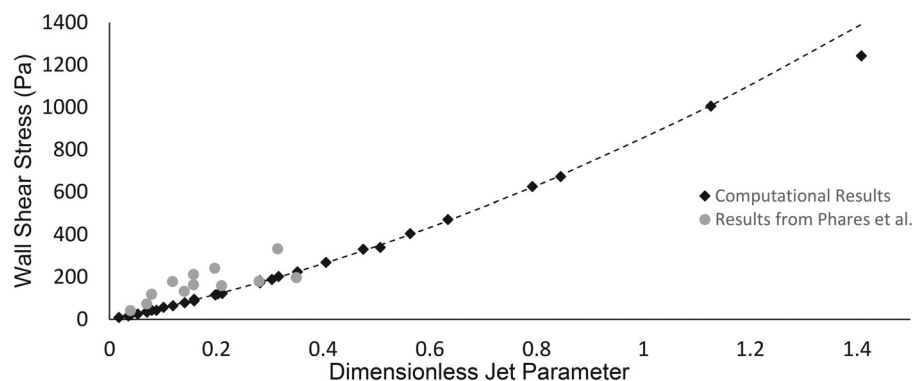
Fig. 11 Plot of the variation of peak wall shear stress with the dimensionless jet parameter with data using the equations developed by Phares et al. [12]
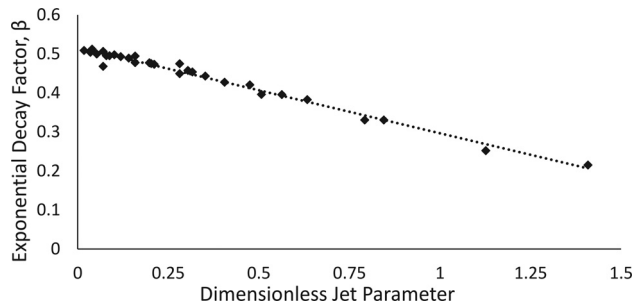
Fig. 13 Effect of dimensionless jet parameter on exponential jet decay factor

The trend line from Fig. 13 gives us Eq. (8), which allows us to determine the decay factor as a function of the DJP

$$\beta = -0.2204 * \text{DJP} + 0.5171 \qquad (8)$$

Using the trends developed for the maximum shear stress along the wall τ_{max}, the maximum shear location r_{max}, and the exponential decay factor β, we can then use Eqs. (6) and (7) as a function of a single variable, DJP, to characterize the entire shear stress profile along the impingement plate for a wide range of underexpanded axisymmetric impinging jets.

4 Conclusion and Discussions

Wall shear stress is used to characterize the forces acting on the particle during its aerodynamic removal; however, a major challenge is the flow-field sensitivity to a variety of parameters: jet pressure, standoff distance, and jet nozzle geometry. Previously published empirical relationships between jet properties and shear stress were validated only in a narrow range of jet operational conditions and do not cover the compressible or supersonic impingement regions. In this publication, we have developed the dimensionless jet parameter that can be used to characterize the wall shear stress profile on the impingement plate for the wide range of flow conditions. The DJP includes two principle components: nozzle pressure to ambient pressure ratio and the nozzle standoff to nozzle diameter ratio. The relationships presented in this work are valid for normal axisymmetric jet. The best agreement for all parameters is obtained when DJP value is directly proportional to the pressure ratio and inversely proportional to $(H/D)^2$. The order of the terms is determined by their relationship to each other. For every factor of X that the pressure is increased, the H/D ratio needs to be increased by a factor of $\sqrt{X}$ to result in similar wall shear stress profiles. It was also found that the diameter of the jet has a slight effect on wall shear stress independently of the DJP. This relationship was found to be accounted for in a simple adjustment such that for a fixed DJP the ratios of shear stress will be proportional to the inverse of the fourth root of the ratio of diameters.

In order to indicate the valid operational conditions for developed relationships, DJP was normalized. The physical representation of DJP = 1 is that the length of the supersonic region of a free (nonimpinging) jet at the given pressure ratio would be equal to the impingement height (or standoff distance) of the jet. At DJP values greater than unity, supersonic flow in the wall jet region is observed experimentally and in the numerical simulations. The presence of the supersonic wall jet significantly complicated the analysis and hence the mapping of wall shear stress is restricted to subsonic flows along the wall jet. As a result, the DJP has been normalized to be in a range of 0–1, beyond which the use of the DJP is not validated for use in locating wall shear stress in Eqs. (5)–(7).

The maximum aerodynamic forces acting on the particle in the boundary layer will be at the location of the maximum shear stress assuming the viscous nonslip wall boundary layer condition.

Finding the maximum values of the wall shear stress and its location is necessary for particle detachment studies and aids in the design of the noncontact sampling devices. The maximum wall shear stress in the subsonic impingement regime can be calculated using the quadratic relationship in Eq. (4). The trend for maximum wall shear stress for lower values of DJP (0–0.2) is nearly linear, and Eq. (4) is dominated by the linear term. This corresponds to incompressible flow along the impingement surface. At higher values of DJP (>0.2) the quadratic term in Eq. (4) is dominant. This term demonstrates that compressible flow along the wall allows for much higher shear stress, and more efficient transfer of shear stress for design criterion tradeoff ($(H/D)^2$ and P_{gauge}/P_{atm}) than incompressible flow.

It was also found that when the DJP is greater than unity, there is a loss of return in the power requirement as the shear stress is limited due to the increase in energy dissipation in the normal (plate) shock wave that forms at the impingement point. In the transitional regime ($1 < \text{DJP} < 2$), the wall stress asymptotically approaches its maximum value limit that can be described by Eq. (3). The maximum increase of the wall stress will be about 150% of the shear stress at DJP = 1. This is not well defined by the relationships developed in this work. In the supersonic wall flow region (DJP > 2), the value of the maximum wall shear stress can be exceeded (though not significantly or predictably). To describe the supersonic wall jet region, additional CFD simulations and experimental validation experiments are needed. The nonslip assumption of the wall flow at the DJP > 1 are not likely to be valid as the flow becomes unstable, which was observed by the high-speed Schlieren visualization. This topic is beyond the scope of this paper. In addition, achieving the supersonic conditions at the surface is not practical for most engineering applications due to power and nozzle standoff requirement.

For DJP < 1, the location of the maximum shear stress was found to be consistent with the jet expansion angle. The radius of the nozzle is subtracted from the radial location of the max shear to account for the shift due to the nozzle geometry. As the DJP approaches zero (low nozzle pressure and larger standoff distance), the peak location approaches the tangent of 7.5 deg, which is a typical value for a spreading angle for subsonic jets. It should also be noted that as the length of the supersonic region approaches the impingement height, the location of the max shear approaches the radius of the jet.

Observing the decay of the wall shear profile from its point of the maximum, an equation led to the derivation of an exponential decay equation. The decay factor for the exponent is also a function of the DJP and, hence, using this similarity parameter, the shear stress along the plate can be mapped for different normally impinging jets.

The limitation of the presented relationship is related to both operational and geometrical considerations. While these results are validated for the normal axisymmetric jet in subsonic impingement scenarios, several parameters can influence the maximum values and location of wall shear stress, as well as the wall shear mapping on the surface. Among these parameters are: (i) high Mach number (> 1) at the impingement location and the presence of shocks at the surface; although these were observed both experimentally and in the CFD simulation, their effect has not been quantified in this work. (ii) Nozzle shape and the nozzle aspect ratio affect flow conditions at the nozzle exit and, thus, will have an impact on the wall shear stress. A nozzle correction factor could be developed in future work to account for over-expanded nozzles. (iii) Jet angle will also have a significant impact on the wall shear stress. For the optimization of removal, it should be ideal to have the jet at a nonperpendicular angle with respect to the impingement plate. The optimum angle will also be developed in future work.

Acknowledgment

Schlieren photography. This work was facilitated though the use of advanced computational, storage, and the networking infrastructure provided by the Hyak supercomputer system at the University of Washington.

Nomenclature

D = diameter of the jet
H = standoff distance of the jet from the plate
P_{atm} = atmospheric pressure (14.7 psi/101,325 Pa)
P_{gauge} = gauge pressure supplied to the jet
r = radial location along the plate
R = radius of the jet ($= D/2$)
β = exponential decay factor
τ = fluidic shear stress

References

[1] Henderson, B., and Powell, A., 1993, "Experiments Concerning Tones Produced By An Axisymmetric Choked Jet Impinging On Flat Plates," J. Sound Vib., **168**(2), pp. 307–326.
[2] Krothapalli, A., Rajkuperan, E., Alvi, F., and Lourenco, L., 1999, "Flow Field and Noise Characteristics of a Supersonic Impinging Jet," J. Fluid Mech., **392**, pp. 155–181.
[3] Tam, C. K. W., and Ahuja, K. K., 1990, "Theoretical Model of Discrete Tone Generation by Impinging Jets," J. Fluid Mech., **214**, pp. 67–87.
[4] Donaldson, C. D., and Snedeker, R. S., 1971, "A Study of Free Jet Impingement—Part 1: Mean Properties of Free and Impinging Jets," J. Fluid Mech., **45**(2), pp. 281–319.
[5] Kalghatgi, G. T., and Hunt, B. L., 1976, "Occurrence of Stagnation Bubbles in Supersonic Jet Impingement Flows," Aeronaut. Q., **27**(3), pp. 169–185.
[6] Alvi, F. S., Ladd, J. A., and Bower, W. W., 2002, "Experimental and Computational Investigation of Supersonic Impinging Jets," AIAA J., **40**(4), pp. 599–609.
[7] Chin, C., Li, M., Harkin, C., Rochwerger, T., Chan, L., Ooi, A., Risborg, A., and Soria, J., 2013, "Investigation of the Flow Structures in Supersonic Free and Impinging Jet Flows," ASME J. Fluids Eng., **135**(3), p. 031202.
[8] Samareh, B., Stier, O., Lüthen, V., and Dolatabadi, A., 2009, "Assessment of CFD Modelling Via Flow Visualization in Cold Spray Process," J. Therm. Spray Technol., **18**(5–6), pp. 934–943.
[9] Young, R. M., Hargather, M. J., and Settles, G. S., 2013, "Shear Stress and Particle Removal Measurements of a Round Turbulent Air Jet Impinging Normally Upon a Planar Wall," J. Aerosol Sci., **62**, pp. 15–25.
[10] Tu, C. V., and Wood, D. H., 1996, "Wall Pressure and Shear Stress Measurements Beneath an Impinging Jet," Exp. Therm. Fluid Sci., **13**(4), pp. 364–373.
[11] Smedley, G. T., Phares, D. J., and Flagan, R. C., 1999, "Entrainment of Fine Particles From Surfaces by Gas Jets Impinging at Normal Incidence," Exp. Fluids, **26**(4), pp. 324–334.
[12] Phares, D. J., Smedley, G. T., and Flagan, R. C., 2000, "The Wall Shear Stress Produced by the Normal Impingement of a Jet on a Flat Surface," J. Fluid Mech., **418**, pp. 351–375.
[13] Keedy, R., Dengler, E., Ariessohn, P., Novosselov, I., and Aliseda, A., 2012, "Removal Rate of Explosive Particles From a Surface by Impingement of a Gas Jet," Aerosol Sci. Technol., **46**(2), pp. 148–155.
[14] Birch, A. D., Hughes, D. J., and Swaffield, F., 1987, "Velocity Decay of Pressure Jets," Combust. Sci. Technol., **52**(1–3), pp. 161–171.
[15] ANSYS, 2012, "14.5 Theory Guide," ANSYS, Inc., Canonsburg, PA.
[16] Miettinen, A., and Siikonen, T., 2015, "Application of Pressure-and Density-Based Methods for Different Flow Speeds," Int. J. Numer. Methods Fluids, **79**(5), pp. 243–267.
[17] Menter, F. R., 1994, "Two-Equation Eddy Viscosity Turbulence Models for Engineering Applications," AIAA J., **32**(8), pp. 1598–1605.
[18] Catalano, P., and Marcello, A., 2003, "An Evaluation of RANS Turbulence Modelling for Aerodynamic Applications," Aerosp. Sci. Technol., **7**(7), pp. 493–509.
[19] Settles, G. S., 2001, *Schlieren and Shadowgraph Techniques: Experimental Fluid Mechanics*, Springer-Verlag, Berlin.